## Appendix B: Energy dependence

A comparison of the number of background counts for all observations used for the analysis of the empty-field regions between the Case 0 and Case 3 datasets has been made. The ratio between the background counts can be seen in Figure B.1. The shaded band depicts the error on the number of background counts estimated from the matched pairs used for the Case 4- and Case 4+ datasets.
The datasets computed for the analysis of the empty-field regions were also divided into bins, such that one bin consists of two energy bins of the original datasets. Then significance histograms were computed for all bins, and a Gaussian fit was performed. The significance histograms as well as the Gaussian fits for all bins for the dataset around Sculptor can be seen in Figure B.2 and Table B.2. The results for the regions around Reticulum II and Tucana II have been summarised in Table B.1 and Table B.3 respectively.

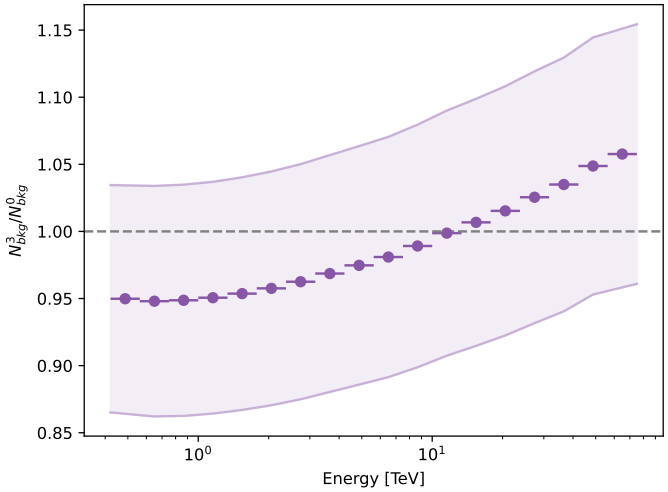


**Fig. B.1.** The ratio between the number of background counts for the Case 0 ($N^0_{BKG}$) and Case 3 ($N^3_{BKG}$) datasets in energy bins. This rate was computed using all observations of the empty-field regions.

**Table B.1.** The fit parameters of the Gaussian fit to the significance distributions estimated from the region around Reticulum II

| Energy bin [TeV] | Case 0 | | Case 3 | | Case 4+ | | Case 4- | |
|---|---|---|---|---|---|---|---|---|
| | $\mu$ | $\sigma$ | $\mu$ | $\sigma$ | $\mu$ | $\sigma$ | $\mu$ | $\sigma$ |
| 0.32 - 0.56 | −0.07 | 1.01 | −0.26 | 1.01 | −0.51 | 1.01 | −0.00 | 1.02 |
| 0.56 - 1.00 | −0.03 | 1.00 | −0.01 | 1.02 | −0.25 | 1.00 | 0.25 | 1.04 |
| 1.00 - 1.78 | −0.12 | 1.04 | −0.02 | 1.05 | −0.18 | 1.04 | 0.14 | 1.07 |
| 1.78 - 3.16 | −0.14 | 1.05 | −0.04 | 1.07 | −0.14 | 1.06 | 0.07 | 1.09 |
| 3.16 - 5.62 | −0.20 | 0.98 | −0.10 | 1.01 | −0.16 | 0.99 | −0.03 | 1.02 |
| 5.62 - 10.00 | −0.30 | 0.78 | −0.24 | 0.80 | −0.27 | 0.80 | −0.21 | 0.78 |

**Table B.2.** The fit parameters of the Gaussian fit to the significance distributions estimated from the region around Sculptor.

| Energy bin [TeV] | Case 0 | | Case 3 | | Case 4+ | | Case 4- | |
|---|---|---|---|---|---|---|---|---|
| | $\mu$ | $\sigma$ | $\mu$ | $\sigma$ | $\mu$ | $\sigma$ | $\mu$ | $\sigma$ |
| 0.18 - 0.32 | −0.13 | 1.01 | −0.12 | 1.02 | −0.37 | 1.00 | 0.14 | 1.06 |
| 0.32 - 0.56 | −0.13 | 1.03 | −0.19 | 1.03 | −0.58 | 1.00 | 0.23 | 1.09 |
| 0.56 - 1.00 | −0.08 | 1.05 | −0.12 | 1.04 | −0.39 | 1.03 | 0.18 | 1.07 |
| 1.00 - 1.78 | −0.15 | 1.06 | −0.18 | 1.06 | −0.36 | 1.03 | −0.02 | 1.09 |
| 1.78 - 3.16 | −0.16 | 1.03 | −0.18 | 1.03 | −0.30 | 1.01 | −0.06 | 1.06 |
| 3.16 - 5.62 | −0.26 | 0.89 | −0.28 | 0.88 | −0.34 | 0.87 | −0.21 | 0.90 |
| 5.62 - 10.00 | −0.27 | 0.67 | −0.28 | 0.67 | −0.32 | 0.66 | −0.25 | 0.68 |

**Table B.3.** The fit parameters of the Gaussian fit to the significance distributions estimated from the region around Tucana II

| Energy bin [TeV] | Case 0 | | Case 3 | | Case 4+ | | Case 4- | |
|---|---|---|---|---|---|---|---|---|
| | $\mu$ | $\sigma$ | $\mu$ | $\sigma$ | $\mu$ | $\sigma$ | $\mu$ | $\sigma$ |
| 0.32 - 0.56 | −0.13 | 1.03 | −0.19 | 1.03 | −0.58 | 1.00 | 0.23 | 1.09 |
| 0.56 - 1.00 | −0.08 | 1.05 | −0.12 | 1.04 | −0.39 | 1.03 | 0.18 | 1.07 |
| 1.00 - 1.78 | −0.15 | 1.06 | −0.18 | 1.06 | −0.36 | 1.03 | 0.02 | 1.09 |
| 1.78 - 3.16 | −0.16 | 1.03 | −0.18 | 1.03 | −0.30 | 1.01 | −0.06 | 1.06 |
| 3.16 - 5.62 | −0.26 | 0.89 | −0.28 | 0.88 | −0.34 | 0.87 | −0.21 | 0.90 |
| 5.62 - 10.00 | −0.27 | 0.67 | −0.28 | 0.67 | −0.32 | 0.66 | −0.25 | 0.68 |

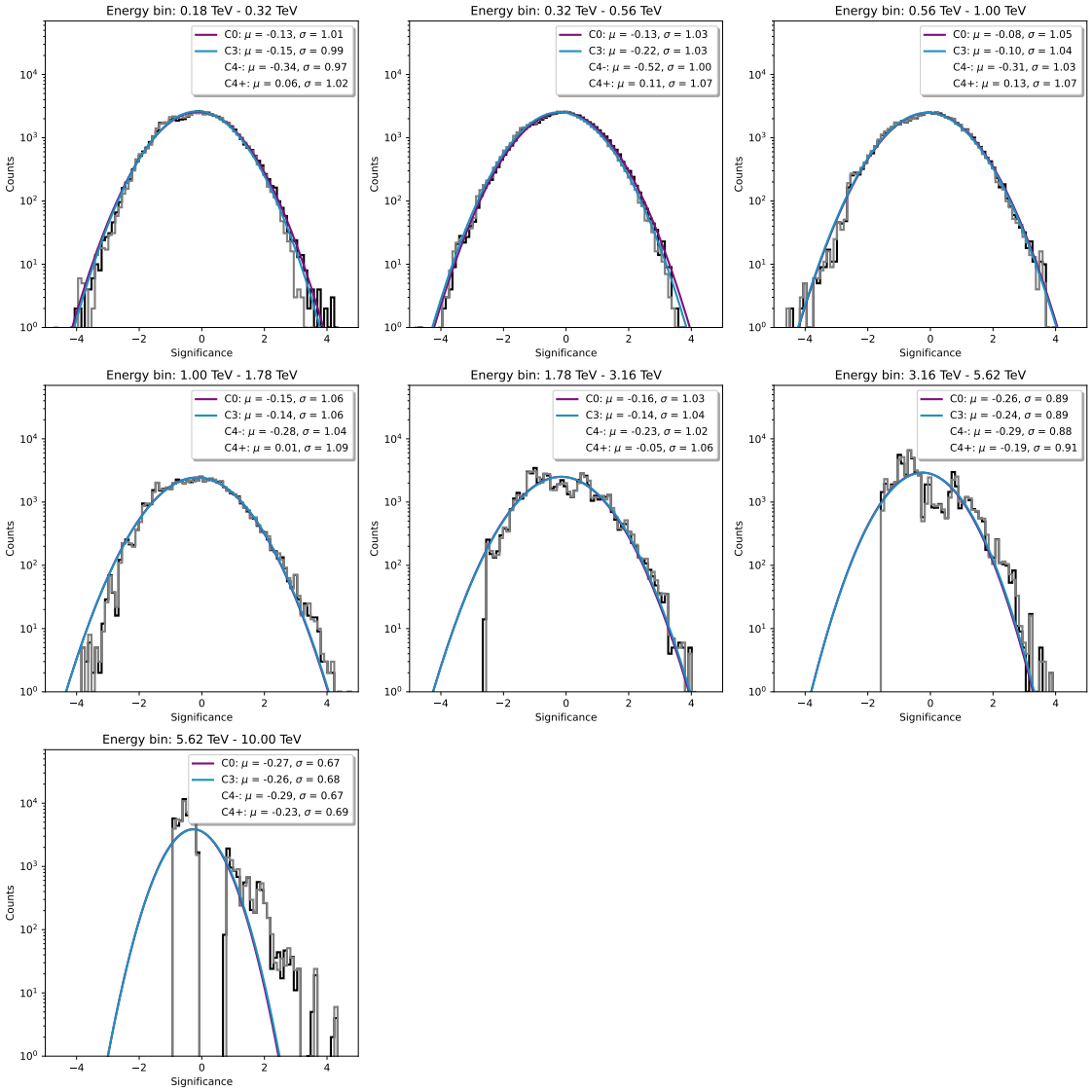


**Fig. B.2.** Significance distribution for the region around Sculptor in energy bins. A Gaussian fit to the histograms for the Case 0 and Case 3 datasets is depicted by the solid lines.

## Appendix C: Fit Results

Table C.1 contains the best-fit values obtained using the background model template and run-matching approaches, for all source regions analysed in this study. Additionally, the best-fit values from Mohrmann et al. (2019) are listed for comparison. Figure C.1, Figure C.2 and Figure C.3 show a visual comparison of the best-fit values including the systematic errors for the regions around the Crab Nebula, PKS 2155−304 and RX J1713.7−3946 respectively.

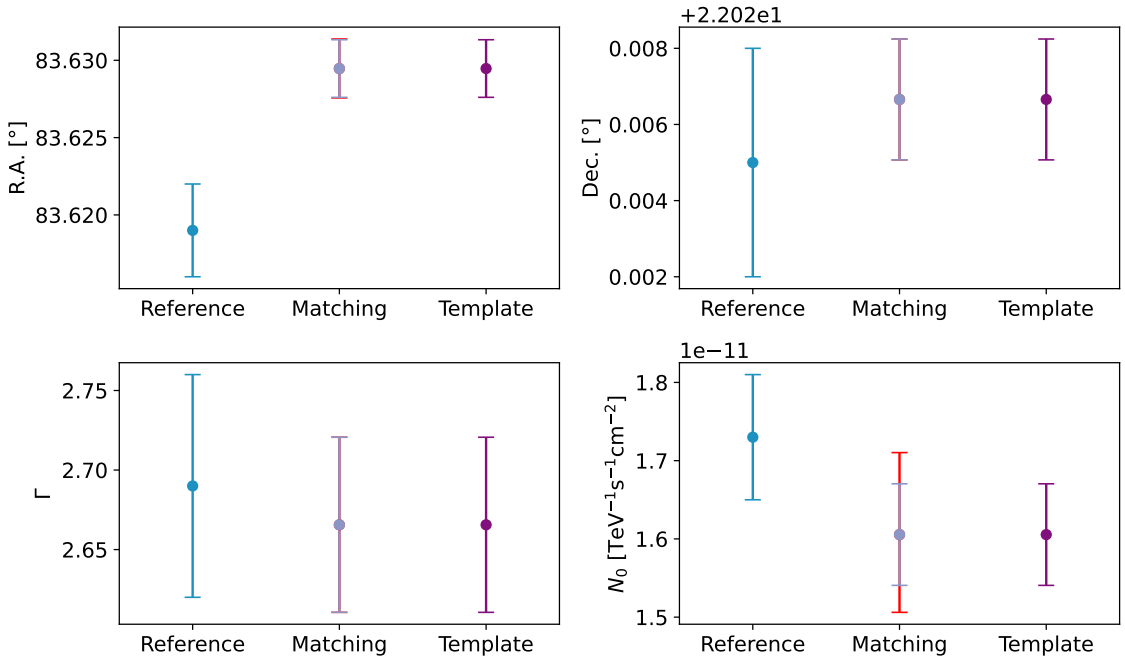


**Fig. C.1.** Comparison between the best-fit values for all parameters of the point model used to describe the emission from the Crab Nebula. The reference values where taken from Mohrmann et al. (2019), Matching refers to the values derived by using the run-matching approach for the background estimation, while template refers to the background model template. The systematics introduced due to the run-matching approach are indicated in red.

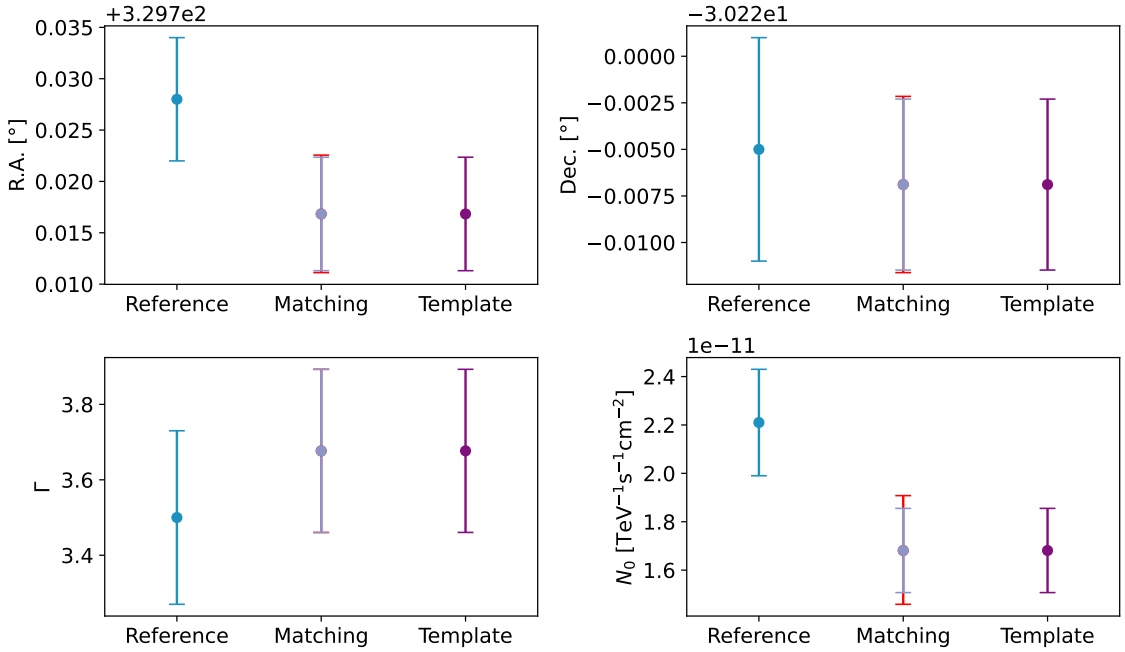


**Fig. C.2.** Comparison between the best-fit values for all parameters of the point model used to describe the emission from PKS 2155−304. The reference values where taken from Mohrmann et al. (2019), Matching refers to the values derived by using the run-matching approach for the background estimation, while template refers to the background model template. The systematics introduced due to the run-matching approach are indicated in red.

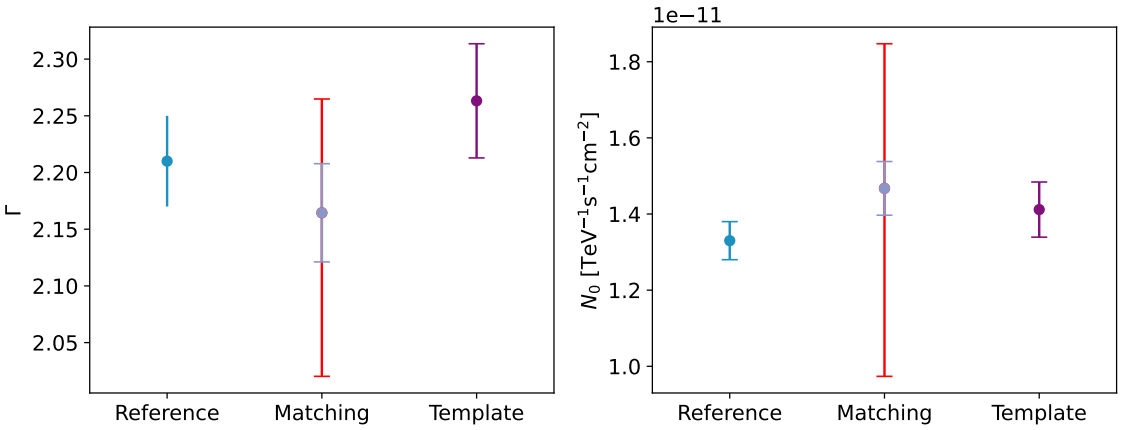


**Fig. C.3.** Comparison between the best-fit values for all fit parameters of the model used to describe the emission from RX J1713.7−3946. The reference values where taken from Mohrmann et al. (2019), Matching refers to the values derived by using the run-matching approach for the background estimation, while template refers to the background model template. The systematics introduced due to the run-matching approach are indicated in red.

**Table C.1.** The best-fit parameters for all sources analysed in this study.

| | | RA [°] | Dec [°] | $r_0$ [°] | $e$ [°] | $\phi$ [°] | $E_0$ [TeV] | $N_0$ [$10^{-12}$ cm$^{-2}$ s$^{-1}$ TeV$^{-1}$] | $\Gamma$ |
|---|---|---|---|---|---|---|---|---|---|
| Crab Nebula | Reference | 83.619 ± 0.003 | 22.025 ± 0.002 | −− | −− | −− | 1.45 | 17.3 ± 0.8 | 2.69 ± 0.07 |
| | Case 0 | 83.628 ± 0.002 | 22.026 ± 0.002 | −− | −− | −− | 1.45 | 16.8 ± 0.7 | 2.73 ± 0.06 |
| | Case 3 | 83.629 ± 0.002 | 22.027 ± 0.002 | −− | −− | −− | 1.45 | 16.1 ± 0.7 | 2.67 ± 0.06 |
| PKS 2155−304 | Reference | 329.73 ± 0.007 | −30.227 ± 0.006 | −− | −− | −− | 0.65 | 22.1 ± 2.2 | 3.50 ± 0.23 |
| | Case 0 | 329.72 ± 0.005 | −30.224 ± 0.004 | −− | −− | −− | 0.65 | 17.1 ± 1.8 | 3.73 ± 0.21 |
| | Case 3 | 329.72 ± 0.006 | −30.227 ± 0.005 | −− | −− | −− | 0.65 | 16.8 ± 1.7 | 3.68 ± 0.2 |
| MSH 15−52 | Reference | 228.55 ± 0.01 | −59.171 ± 0.007 | 0.196 ± 0.007 | 0.801 ± 0.038 | 151 ± 6.0 | 1.4 | 2.91 ± 0.14 | 2.41 ± 0.05 |
| | Case 0 | 228.56 ± 0.04 | −59.175 ± 0.003 | 0.170 ± 0.004 | 0.739 ± 0.020 | 145.4 ± 2.2 | 1.4 | 3.35 ± 0.24 | 2.42 ± 0.08 |
| | Case 3 | 228.56 ± 0.02 | −59.170 ± 0.001 | 0.169 ± 0.001 | 0.765 ± 0.034 | 149 ± 7.8 | 1.4 | 3.26 ± 0.34 | 2.40 ± 0.08 |
| RX J1713.7−3946 | Reference | −− | −− | −− | −− | −− | 1.15 | 13.3 ± 0.5 | 2.21 ± 0.04 |
| | Case 0 | −− | −− | −− | −− | −− | 1.15 | 14.1 ± 0.7 | 2.26 ± 0.05 |
| | Case 3 | −− | −− | −− | −− | −− | 1.15 | 14.9 ± 0.7 | 2.17 ± 0.04 |

**Note:** The parameters $r_0$, $e$, $\Phi$ are the major axis, eccentricity, and position angle of the elliptical disk used to describe the emission from MSH 15−52. These fit parameters are compared to reference values from Mohrmann et al. (2019). The reference energy $E_{\rm ref}$ was fixed for the likelihood-minimisation.

## Appendix D: Additional significance maps and spectra

Here we show the significance maps and distributions of the region around PKS 2155−304 (Figure D.4), MSH 15−52 (Figure D.5) and RX J1713.7−3946 (Figure D.6). Although a small shift in the background distributions for the datasets estimated using the run-matching approach can be observed, this shift is within the systematic uncertainty (see Table 6).
The SED estimated for the Crab Nebula, PKS 2155−304 and MSH 15−52 are shown in Figures D.1, D.2 and D.3 respectively. The lower panel of these figures shows the deviation between the two sets of fluxpoints and the best-fit spectral model derived in the analysis of the respective Case 3 datasets, defined by $(x_{1/2} - x_{model})/x_{model}$, with $x_1$ the differential energy flux in the respective energy bin for the reference fluxpoints derived in Mohrmann et al. (2019), $x_2$ the differential energy flux for the fluxpoints derived from the Case 3 datasets and $x_{model}$ the differential energy flux estimated from the best-fit spectral model.

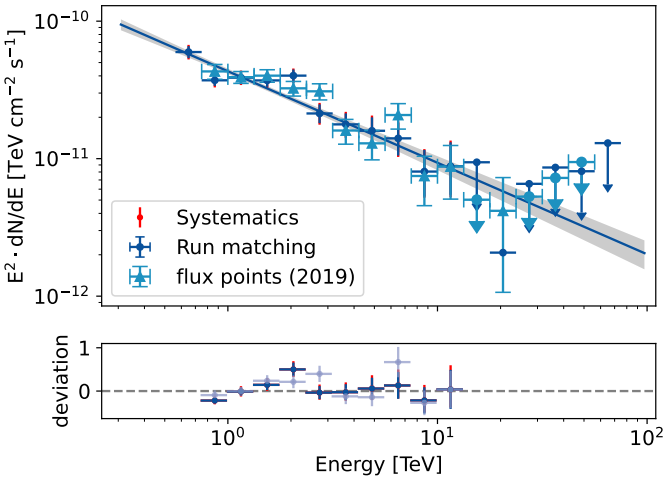


**Fig. D.1.** SED of the Crab Nebula using the run-matching approach for the background estimation compared to the reference SED from (Mohrmann et al. 2019). The deviation between the two SEDs and the best-fit model derived for the Case 3 datasets is depicted in the lower panel.

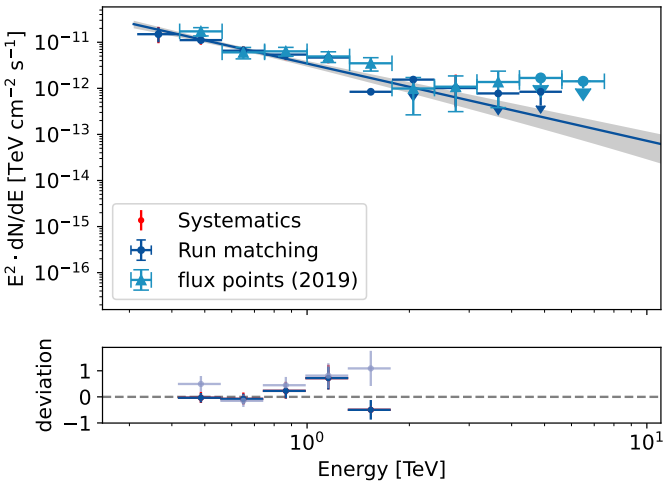


**Fig. D.2.** As in Fig. D.1 for PKS 2155−304

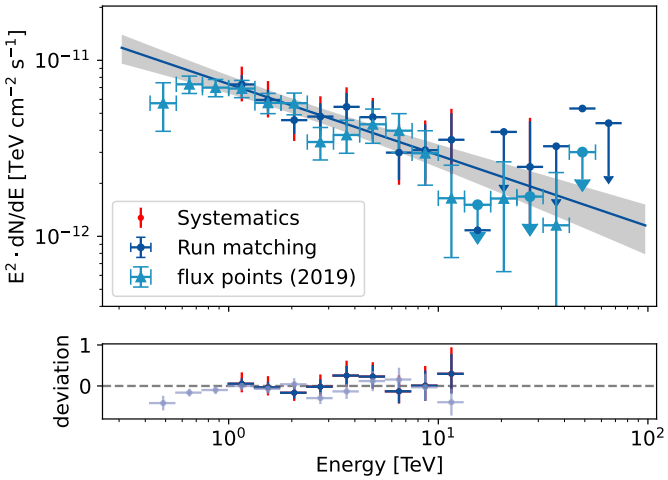


**Fig. D.3.** As in Fig. D.1 for MSH 15−52

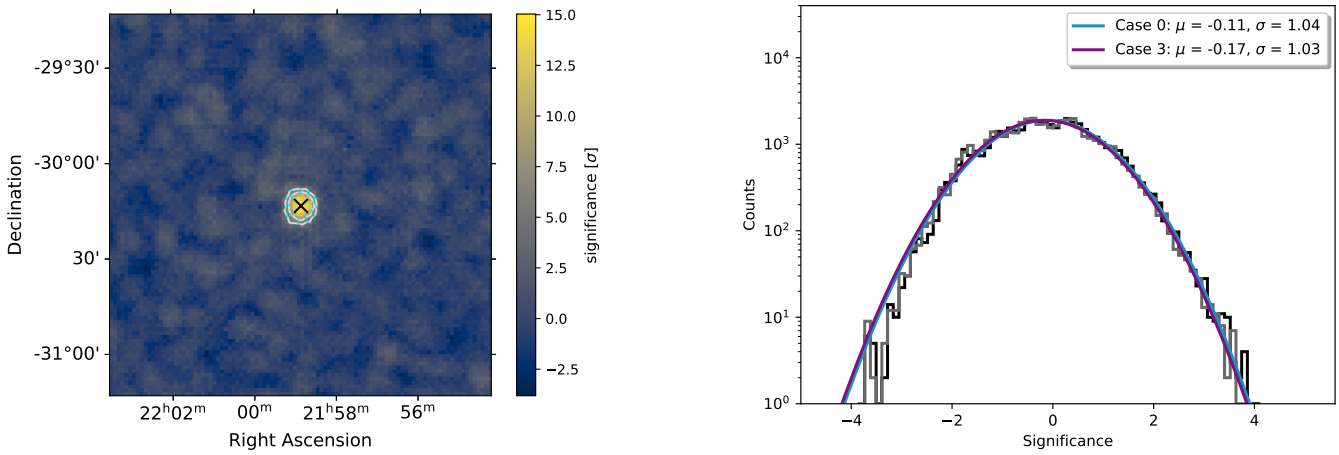


**Fig. D.4.** Left: Li&Ma significance map of the region around PKS 2155−304, with 5 $\sigma$ and 8 $\sigma$ contours, from the Case 0 dataset (blue), and from the Case 3 dataset (pink). The best-fit position is indicated by the black cross. Right: significance distribution of the background in the FoV around PKS 2155−304 for both background estimation techniques, fit with a normal distribution.

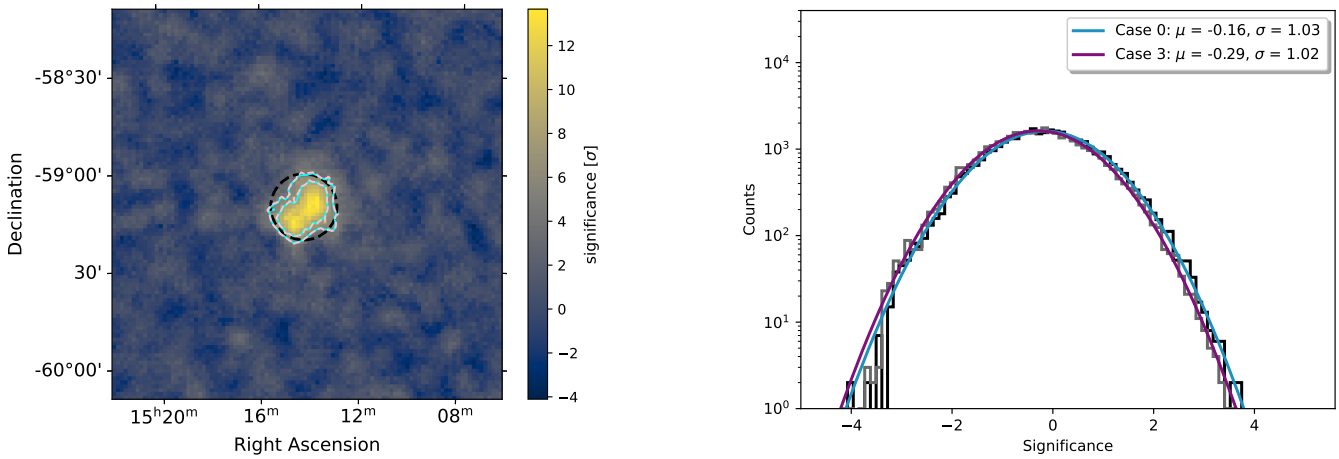


**Fig. D.5.** Left: Li&Ma significance map of the region around MSH 15−52, with 5 $\sigma$ and 8 $\sigma$ contours from the Case 0 dataset (blue) and from the Case 3 dataset (pink). The best-fit morphology is indicated by the black-dashed line. Right: The significance distribution of the background in the FoV for both background estimation techniques, fit with a normal distribution.

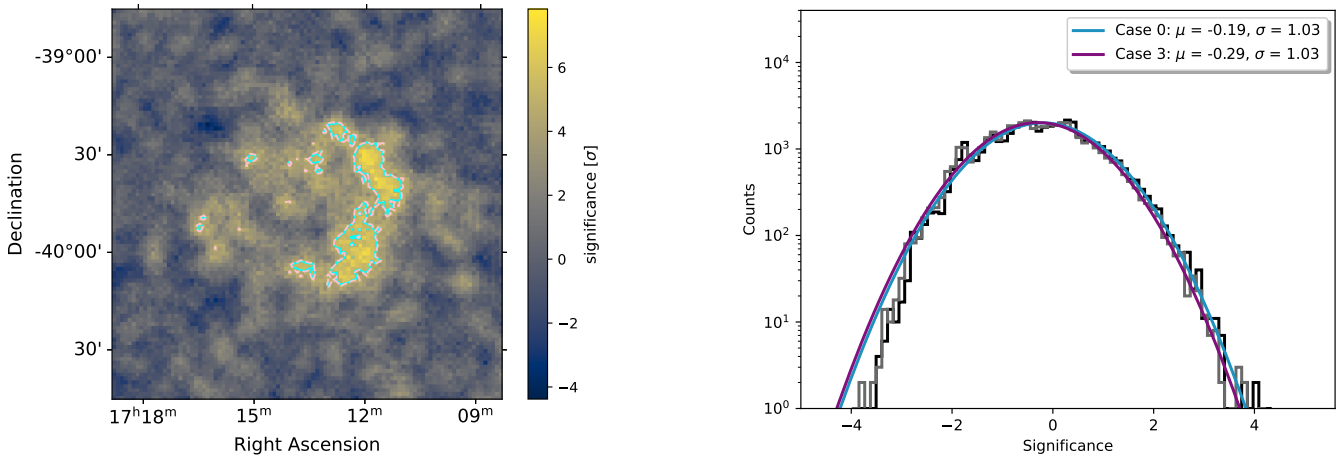


**Fig. D.6.** Left: Li&Ma significance map of the region around RX J1713.7−3946, with 5 $\sigma$ and 8 $\sigma$ contours for Case 0 (blue), and for Case 3 (pink). Right: significance distribution of the background in the FoV for both background estimation techniques, fit with a normal distribution.